

RESEARCH ARTICLE

Modeling of a Soft Robotic Tongue Driven by Compressed Air

XUANMING LU¹, WEILIANG XU², (Senior Member, IEEE), AND XIAONING LI³¹Industrial Technology Research Institute of Intelligent Equipment, Nanjing Institute of Technology, Nanjing 211167, China²Department of Mechanical Engineering, University of Auckland, Auckland 1010, New Zealand³School of Mechanical Engineering, Nanjing University of Science and Technology, Nanjing 210094, China

Corresponding author: Xuanming Lu (garylxm@njit.edu.cn)

This work was supported in part by the Jiangsu Education Department under Grant 20KJB460022, and in part by the Nanjing Institute of Technology under Grant YKJ202045.

ABSTRACT A novel soft robotic tongue is proposed for the purpose of presenting typical tongue movements in speaking, which is pneumatically actuated and supposed to be applied in pronunciation teaching device and humanoid robot to gain verisimilitude. The actuation and control system is mainly composed of solenoid proportional valves (ITV0010, SMC, Japan), DAQ card (PCIE6321, NI, USA) and motion tracking system (OptiTrack, NaturalPoint, USA). A theoretical model based on continuum mechanics is established building the relationship between input air pressure and output deformation. On the basis of the proposed theoretical model and Artificial Neural Network (ANN), an integrated control algorithm is preliminarily raised for different purpose of use in static and dynamic control. A series of verification experiments are carried out based on OptiTrack system in order to test motion controllability and working performance of the robotic tongue. The experimental results indicate that the proposed theoretical model is more suitable for static shape control due to obvious deformation delay compared with input air pressure. High deformation repeatability guarantees the precision of ANN based control method which is more suitable for dynamic motion control. The results of performance test show that actual movements of the robotic tongue generally meet the demand in demonstrating tongue shape when speaking.

INDEX TERMS Soft robot, tongue, theoretical model, motion tracking.

I. INTRODUCTION

Robotic tongue plays an important role of verisimilitude improvement in pronunciation teaching device and humanoid robot [1]. For the hearing impaired, robotic tongue can show tongue shapes more visually during pronunciation teaching and training process. Besides, if a robotic tongue can be mounted into the mouth of a humanoid robot and move along with the opening & closing of the mouth during speaking, such humanoid robot will acquire more verisimilitude. However, due to insufficient understanding of the role played by robotic tongue and existing technological difficulties, there has been no product to meet such kind of demand, which brings inconvenience to the hearing impaired during pronunciation training, and causes the lack of verisimilitude of humanoid robot when speaking.

The associate editor coordinating the review of this manuscript and approving it for publication was Claudia Raibulet¹.

Owing to complicated structure and motion of the tongue, there have been very few devices which can only partly mimic mechanical functions of human tongue so far. A multi-degree of freedom (DOF) flexible robotic tongue was proposed by Kawamura et al. and several typical tongue movements were achieved [2]. A three dimensional robotic tongue with liquid sealing mechanism was developed to improve sound production in a talking robot [3], [4]. Nevertheless, these two devices both contain rigid structure and lack sufficient flexibility, which are far different from biological tongues.

Soft robots refer to a sort of robots or actuators which do not contain rigid structure. They are made of different materials such as SMA (Shape Memory Alloy), dielectric elastomer (DE), paper and silicone rubber for different purpose of use [5], [6], [7], [8], [9], [10], [11], [12], [13], [14], [15], [16], [17], [18], [19], [20], and applied in fields such as bionics [8], [13], [14], medical science [15] and even in rescue [16] due to the soft property and ability of

forming large deformation. Pneu-Net [17] is one of the most commonly used structural patterns in soft robotics. Pneu-Net based robot is usually composed of multiple layers. The difference in strain between these layers causes bending deformation. Based on this structure, a series of robots have been proposed including multigait robot [18], chemical reagent transportation robot [19], soft gripper [11], [20] and biomimetic fish [13]. However, strong nonlinearity of soft materials combining with pneumatic actuation pattern brings much more challenges in modelling and controlling soft robots compared with traditional motor-driven counterparts.

There have been some breakthroughs in modelling and controlling soft robots so far [21], [22], [23], [24]. Due to the nonlinearity, complexity and uncertainty of the robotic system, most of the proposed models are only suitable for specific robotic systems, not universal to all. Polygerinos et al proposed a theoretical model for a Pneu-Net based robot to reveal the relationship between input air pressure and output bending angle [21]. Nevertheless, for the reason that this model only pays attention to bending deformation, it is merely suitable for basic 2D bending actuators with strip shape.

Aiming to meet the requirements in pronunciation teaching device and humanoid robot, a soft robotic tongue system is proposed to demonstrate tongue motions during speaking. The rest of the paper is organized as follows. Technical demand, structure and pneumatic actuation system are generally described in section II. In section III, a theoretical model is introduced to investigate the relationship between input air pressure and output deformation in simple motions including roll-up, roll-down and elongation, based on which the control scheme is preliminarily set up. The controllability and performance of the robotic tongue is experimentally tested in section IV. Discussions as well as future work plan are concluded in section V.

II. DESIGN OF SOFT ROBOTIC TONGUE

The robotic tongue system contains two parts: tongue body and pneumatic actuation system. The body of the robotic tongue is based on biological tongue with Pneu-Net structure and totally soft without any skeletal support. The pneumatic system also provides compliant actuation pattern for the robotic tongue.

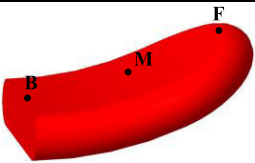
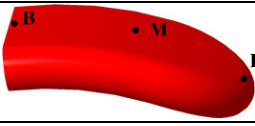
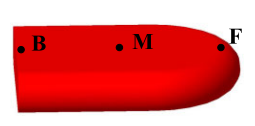
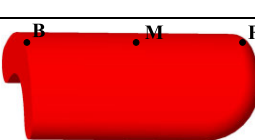
In previous work, the structure and actuation system were proposed [25], [26], [27], [28]. Through comparison and analysis according to the performance of the robotic tongue, layer structure, geometrical parameters and chamber arrangement are adjusted, and solenoid proportional valves are used instead of directional valves. The latest design is presented as follows.

A. TONGUE MOVEMENTS IN SPEECH

The muscular structure of human tongue is mainly composed of extrinsic and intrinsic muscles. The extrinsic muscles extend outside the tongue and move it bodily, while the

intrinsic muscles are wholly within the tongue body with layer structure altering tongue shape [29].

TABLE 1. The geometrical parameters of three key points (B, M and F) corresponding to four deformation types.

Deformation Type	The Position of Key Points	Geometrical Parameters of Key Points
Roll-up		The maximum resultant displacement of Point F should be between 19.2 mm to 23.0 mm.
Roll-down		The maximum resultant displacement of Point F is 18.3 mm.
Elongation		The maximum elongation deformations are 8.3 mm (Point F), 6.1 mm (Point M) and 5.1 mm (Point B).
Groove		The maximum resultant displacement of Point B is about 10 mm.

The movements of tongue in speech is complicated, however, these can be split into the combinations of a series of basic movements including roll-up, roll-down, elongation and groove [30], [31], [32], [33]. For convenience of measurement, four types of basic movements are further simplified to the displacement of 3 key points (B, M & F) on the surface of the robotic tongue (shown in TABLE 1). Due to individual difference, experimental method and measuring error, the measurement results vary among different tests. By analyzing, classifying and summarizing the data from [32], [33], [34], [35], and [36], the geometrical parameters of three key points (B, M and F) corresponding to four deformation types are shown in TABLE 1.

B. STRUCTURE OF THE ROBOTIC TONGUE

The robotic tongue is supposed to be mounted in the mouth of a humanoid robot or a pronouncing demonstration device. In order to gain verisimilitude, the structural design of robotic tongue should basically conform to the biological structure of human tongue. Also, the movements that the robotic tongue can achieve should meet the basic demand in speech. Consequently, the robotic tongue is simplified from a biological tongue with similar size (length l of 34.95 mm, breadth d of 43.7 mm and thickness h of 10.6 mm, shown in Fig. 1(b)). Mimicking the structure of intrinsic muscles, the robotic tongue consists of three layers including two extensible layers made of silicone rubber—Ecoflex 0030 (Smooth-On, USA) on either side and one less extensible layer made of PDMS (DOWSIL, USA) in the middle. Six sets of chambers

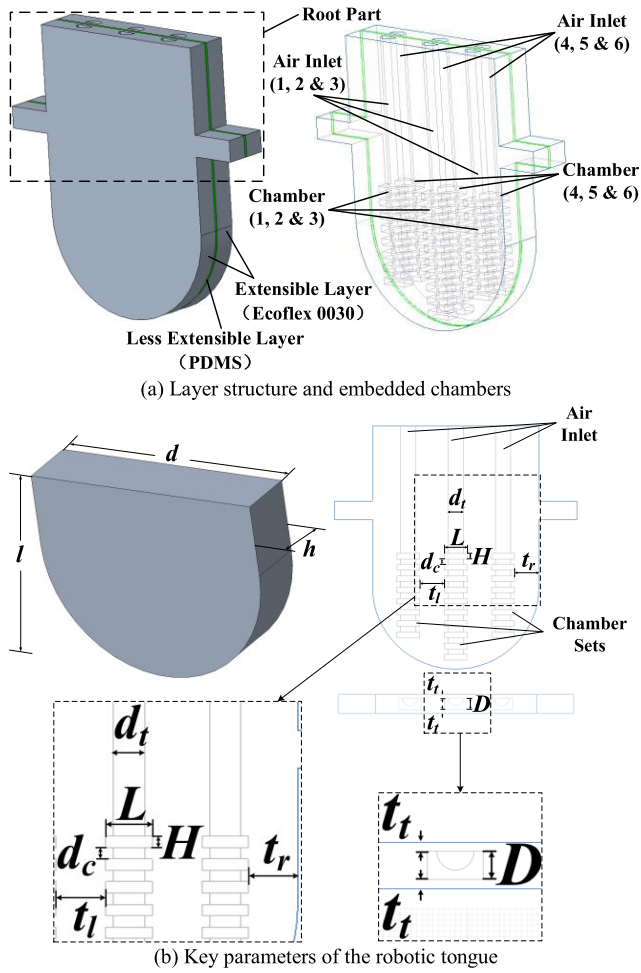


FIGURE 1. The structure of robotic tongue.

(Chamber 1 to 6) are embedded in two extensible layers in total, with three in either layer. Each set is composed of a series of sub-chambers and equipped with an airway (Air Inlet 1 to 6) for air supply. A root part which does not take part in the deforming process when chambers are pressurized is designed for the fixation of the robotic tongue. The whole structure of the robotic tongue is shown in Fig. 1(a). Key parameters in Fig. 1(b) are $d = 43.7$ mm, $l = 34.95$ mm, $h = 10.6$ mm, $L = 6$ mm, $H = 1.5$ mm, $D = 3$ mm, $d_t = 4$ mm, $d_c = 1.5$ mm, $t_r = t_l = 6.425$ mm, $t_t = 1$ mm. The size of the robotic tongue body is defined by d , l and h . The size of each sub-chamber is defined by D , L and H . The relative location of the chambers inside the tongue body is defined by t_l , t_r and t_t . The distance between two sub-chambers is d_c . The width of air inlet is d_t . All these parameters are further discussed when modelling in Section III.

The robotic tongue is fabricated through casting with 3D printed moulds at room temperature. Each layer of the robotic tongue is made separately using their own corresponding moulds. Then these layers are bonded together in a specific order making up the whole robotic tongue body. Finally, silicone tubes are plugged into the airways which are sealed

at the entrance. For the purpose of acquiring better sealability, only Ecoflex 0030 itself is used as adhesive when bonding the layers and sealing the airways. Air tight test of different sets of chambers is carried out before use.

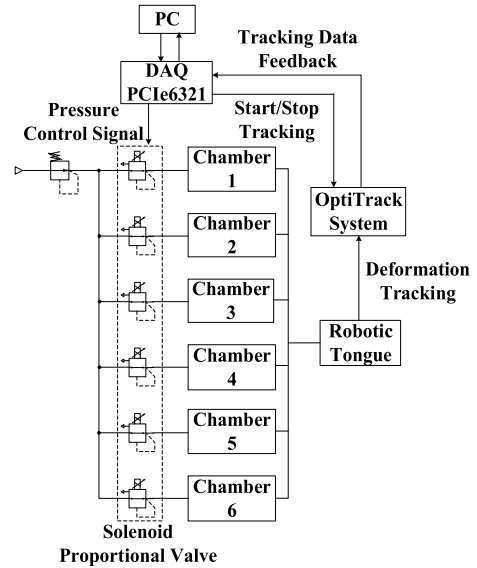


FIGURE 2. The actuation and control system of soft robotic tongue.

C. ACTUATION AND CONTROL SYSTEM

The actuation and control system mainly contains air source, solenoid proportional valves (ITV0010), motion tracking system (OptiTrack), DAQ card (PCIe6321) and PC. The whole system is shown in Fig. 2. The actuation part of the system is a typical pneumatic circuit which includes air compressor, air cleaner, valves, pipes and some other accessories. Normal air is compressed through air compressor, filtered through air cleaner and then inlet to air chambers after pressure regulation through specific valves.

During the working process, six sets of chambers (shown in Fig. 1(a)) are pressurized through six solenoid proportional valves forming different deformation patterns. The deformation is captured by OptiTrack system and sent to PC through PCIe6321. Based on the data obtained from OptiTrack system, control signal is generated in PC and sent to solenoid proportional valves through PCIe6321 for the purpose of regulating the output pressure from valves as well as the deformation of the robotic tongue. Detailed control algorithm is described below in Section III-C.

Based on the layer structure and actuation system, four types of deformation are realized including three simple types (roll-up, roll-down and elongation) and one complicated type (groove) corresponding to four typical tongue shapes in TABLE 1.

III. THEORETICAL MODEL OF THE ROBOTIC TONGUE

A geometrical model based on surface reconstruction method was proposed in previous work [25], [26], [27], [28] to

describe the deformed surface of the robotic tongue quantitatively. However, only the geometrical shape of the robotic tongue during deformation was involved in this model. The relationship between input air pressure in chambers and output tongue shape was not considered, which is crucial to motion control of the robotic tongue.

For the purpose of better understanding deformation characteristics of the robotic tongue and preparing for motion control, a theoretical model based on continuum mechanics is proposed to demonstrate the relationship between input air pressure and output deformation. Two types of model are included respectively for two simple deformation types which are elongation and roll (roll-up and roll-down). Compared with the external force caused by compressed air, other forces (e.g. gravity, friction) are ignored. The PDMS layer in the middle does not contain any chamber or airway, merely constrains the Ecoflex layer causing bending deformation, which means that it does not participate in the actuation process. Besides, the thickness of PDMS layer is much thinner than that of Ecoflex layer. Thus the PDMS layer is neglected. In addition, the airways and fixed root part are not taken into consideration as well. For the reason that the change of geometrical parameters during deformation is far smaller compared with the initial parameters, size change of the robotic tongue is not taken into consideration and the initial parameters are used when modelling.

A. MODEL FOR ELONGATION DEFORMATION

Elongation refers to a simple type of deformation along the longitudinal direction just like the biological tongue elongating out of mouth. The robotic tongue is capable of elongating when all six sets of chambers are pressurized. This theoretical model aims to find the relationship between input air pressure P in chambers and output elongation λ compared with the unpressurized state.

All six sets of chambers are pressurized causing the robotic tongue to elongate. For each set of chamber, there are a series of sub-chambers. When all sub-chambers are pressurized, the forces on adjacent sub-chambers are counteracted. Only the force on both ends results in the elongation of the robotic tongue.

Based on the theory of continuum mechanics, Mooney-Rivlin strain-energy function model is chosen to set up the mechanical model of the robotic tongue. For Ecoflex 0030, two main material parameters of Mooney-Rivlin model C_1 and C_2 are calculated by

$$C_1 = \frac{E_{Ecoflex}}{5(1 + \nu_{Ecoflex})}, C_2 = \frac{1}{4}C_1 \quad (1)$$

where the Young's modulus $E_{Ecoflex} = 60$ kPa and Poisson's ratio $\nu_{Ecoflex} = 0.49$ are derived from [37]. The strain-energy function W of Mooney Rivlin model is expressed as

$$W(I_1, I_2) = C_1(I_1 - 3) + C_2(I_2 - 3) \quad (2)$$

in which I_1 and I_2 are the invariants of left Cauchy-Green deformation tensor \mathbf{B} . It is assumed that the deformation is

homogeneous, thus the left Cauchy-Green deformation tensor \mathbf{B} can be represented by the diagonal matrix shown in Eqs. 3.

$$\mathbf{B} = \begin{bmatrix} \lambda_1^2 & 0 & 0 \\ 0 & \lambda_2^2 & 0 \\ 0 & 0 & \lambda_3^2 \end{bmatrix} \quad (3)$$

$$\begin{cases} I_1 = tr(\mathbf{B}) = \lambda_1^2 + \lambda_2^2 + \lambda_3^2 \\ I_2 = \frac{1}{2} \{ [tr(\mathbf{B})]^2 - tr(\mathbf{B}^2) \} = (\lambda_1\lambda_2)^2 \\ \quad + (\lambda_2\lambda_3)^2 + (\lambda_1\lambda_3)^2 \\ I_3 = det(\mathbf{B}) = (\lambda_1\lambda_2\lambda_3)^2 \end{cases}$$

In Eqs. 3, λ_1 , λ_2 and λ_3 represent three principal stretches. For the reason that Ecoflex 0030 is a typical kind of incompressible hyperelastic material, the internal constraint is expressed as

$$I_3 = (\lambda_1\lambda_2\lambda_3)^2 = 1 \rightarrow \lambda_1\lambda_2\lambda_3 = 1. \quad (4)$$

The constitutive relation of incompressible hyperelastic material is shown as

$$\boldsymbol{\sigma} = -p\mathbf{I} + 2\frac{\partial W}{\partial I_1}\mathbf{B} - 2\frac{\partial W}{\partial I_2}\mathbf{B}^{-1} \quad (5)$$

where $\boldsymbol{\sigma}$ is the Cauchy stress tensor, p stands for the hydrostatic pressure, and \mathbf{I} represents the unit tensor. From Eqs. 3 and Eq. 5, the Cauchy stress is presented as

$$\sigma_i = 2 \left(\lambda_i^2 \frac{\partial W}{\partial I_1} - \frac{1}{\lambda_i^2} \frac{\partial W}{\partial I_2} \right) - p, \quad i = 1, 2, 3 \quad (6)$$

from which it is calculated that

$$\sigma_1 - \sigma_3 = 2 \left(\lambda_1^2 \frac{\partial W}{\partial I_1} - \frac{1}{\lambda_1^2} \frac{\partial W}{\partial I_2} - \lambda_3^2 \frac{\partial W}{\partial I_1} + \frac{1}{\lambda_3^2} \frac{\partial W}{\partial I_2} \right). \quad (7)$$

Corresponding to the stretches (λ_1 , λ_2 and λ_3), σ_1 , σ_2 and σ_3 represent the axial, circumferential and radial stress respectively. For uniaxial elongation, there is no obvious circumferential and radial stress, thus the Cauchy stress and elongation can be expressed as

$$\sigma_1 = \sigma, \sigma_2 = \sigma_3 = 0, \lambda_1 = \lambda, \lambda_2 = \lambda_3 = \frac{1}{\sqrt{\lambda}}. \quad (8)$$

From Eq. 7 and Eqs. 8, the axial stress σ is shown as

$$\sigma_1 = \sigma = 2 \left(\lambda^2 - \frac{1}{\lambda} \right) \left(\frac{\partial W}{\partial I_1} + \frac{1}{\lambda} \frac{\partial W}{\partial I_2} \right). \quad (9)$$

By taking the derivative of the strain-energy function (Eq. 2), it is found that

$$\frac{\partial W}{\partial I_1} = C_1, \frac{\partial W}{\partial I_2} = C_2. \quad (10)$$

Then substituting Eqs. 10 into Eq. 9, the axial stress σ is presented as

$$\sigma = 2 \left(\lambda^2 - \frac{1}{\lambda} \right) \left(C_1 + \frac{1}{\lambda} C_2 \right). \quad (11)$$

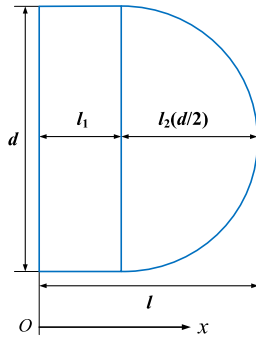


FIGURE 3. Geometric parameters in elongation deformation.

As the expression of the axial stress corresponding to elongation is obtained, the next step is to establish the equilibrium equation using the axial stress and input air pressure. The shape of the robotic tongue body without fixed root part is simplified to a half-cylinder at the apex and a cuboid at the posterior. Key geometric parameters of the robotic tongue body are shown in Fig. 1(b). The Width d is 43.7 mm at the posterior part, the total length l is 34.95 mm including the posterior length l_1 of 13.1 mm and the apex length l_2 of 21.85 mm. Besides, the tongue thickness h (10.6 mm) and the size of one sub-chamber ($L = 6$ mm, $H = 1.5$ mm, $D = 3$ mm) are obtained from Fig. 1(b). Along the length direction, the origin of x axis is set to the end of the posterior part (shown in Fig. 3). At the posterior part ($0 < x < 13.1$), the width remains unchanged (43.7 mm). At the apex part ($13.1 < x < 34.95$), the width decreases gradually due to the half-cylinder geometry. The average width along the length direction is calculated as

$$\bar{d} = \frac{\int_0^{l_1} dx + \int_{l_1}^l 2\sqrt{\left(\frac{d}{2}\right)^2 - (x - l_1)^2} dx}{l}. \quad (12)$$

Considering the relationship between the stress, external force and cross sectional area, the equilibrium equation can be expressed as

$$\sigma = \frac{\left(\sum_{i=1}^6 P_i\right) \cdot (L \cdot D)}{h \cdot \bar{d}}, \lambda > 1 \quad (13)$$

in which P_i stands for the air pressure in each chamber set. Through simultaneous equations (Eq. 11 and Eq. 13), the relationship between input air pressure P and output elongation λ is acquired.

B. MODEL FOR ROLL DEFORMATION

Besides elongation, rolling upwards and rolling downwards (roll-up and roll-down for short) are other two main motions of human tongue. In order to realize the roll deformation, three of six sets of chambers on either side are pressurized simultaneously. Due to the difference in strain of the Ecoflex layer and PDMS layer, the robotic tongue is able to bend towards the side on which the chambers are not pressurized.

The theoretical model is proposed to describe the relationship between input air pressure P and output bending angle θ of the deformed tongue.

Similar to elongation, Mooney-Rivlin strain-energy function model is used in roll deformation. For roll-up and roll-down, there is no obvious twisting deformation along the circumferential direction, thus the circumferential strain is ignored. If the axial elongation (along the length l direction) λ_1 is defined as λ , the radial deformation (along the thickness h direction) λ_3 is acquired as $1/\lambda$ due to Eq. 4 and $\lambda_2 = 1$. The principal nominal stresses s_i is expressed as

$$s_i = \frac{\partial W}{\partial \lambda_i} - \frac{a}{\lambda_i}, i = 1, 2, 3 \quad (14)$$

in which a represents the Lagrange multiplier. If the deformation along the thickness direction is ignored, the radial nominal stress s_3 is assumed to be 0, that is

$$s_3 = \frac{\partial W}{\partial \lambda_3} - \frac{a}{\lambda_3} = 0. \quad (15)$$

Through simultaneous equations (Eq. 2, Eqs. 3 and Eq. 15), the Lagrange multiplier a is obtained (Eq. 16).

$$a = 2\lambda_3^2(C_1 + C_2\lambda_1^2 + C_2\lambda_2^2) \quad (16)$$

Then substituting Eq. 16 into Eq. 14, the axial nominal stress s_1 is acquired (Eq. 17).

$$s_1 = 2C_1\lambda + 2C_2\lambda + \frac{2C_2}{\lambda} - \frac{2(C_1 + C_2 + C_2\lambda^2)}{\lambda^3} \quad (17)$$

Taking roll-down for instance, the roll deformation is considered to be pure bending. Aiming to establish the torque equilibrium using the axial nominal stress s_1 and input air pressure, the first step is to calculate the internal torque caused by material resistance using the mechanical properties of Ecoflex material. There are $n = 26$ sub-chambers involved in roll-down deformation. For all these sub-chambers, the thicknesses of four walls on the top, bottom, left and right are the same with $t_t = 1$ mm, $t_b = 6.6$ mm, $t_l = 6.425$ mm and $t_r = 6.425$ mm respectively (shown in Fig. 4(a), the other three sets of chambers and the PDMS layer in the middle are neglected). The radius of the deformed tongue is defined as r . A point Q is set with a distance of t from the bottom (shown in Fig. 4(b)). The axial elongation is expressed as

$$\lambda = \frac{t + r}{r}. \quad (18)$$

The moment caused by material resistance against air pressure in chambers (M_s) is decomposed to the moments combining top (M_t), bottom (M_b), left (M_l) and right (M_r) walls (Eqs. 19).

$$\begin{aligned} M_t &= n \cdot \int_{t_b+D}^h L \cdot H \cdot (t + t_b + D + r) \cdot s_1 dt \\ M_b &= n \cdot \int_0^{t_b} L \cdot H \cdot (t + r) \cdot s_1 dt \\ M_l &= M_r = n \cdot \int_0^h t_l \cdot H \cdot (t + r) \cdot s_1 dt \\ M_s &= M_t + M_b + M_l + M_r \end{aligned} \quad (19)$$

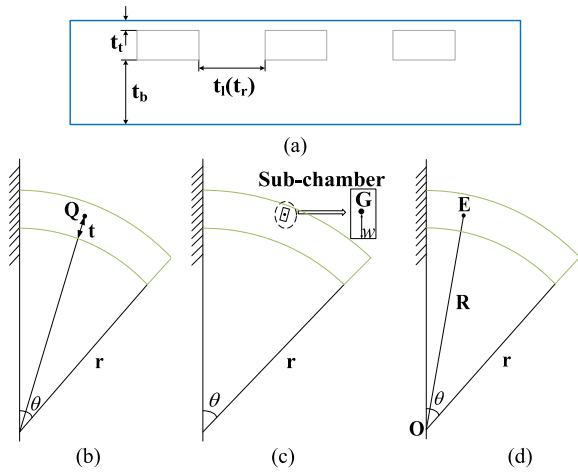


FIGURE 4. (a) The thickness of four walls around the chamber; (b), (c) & (d) The position of key points Q, G and E inside the robotic tongue body.

The second step is to acquire the moment caused by the air pressure in chambers. Only three sets of chambers are pressurized in the deformation of roll-down. Similar to the elongation model, the forces between two adjacent sub-chambers are counteracted, thus only those pressures in sub-chambers on both ends are considered. The moment generated by input air pressure is expressed as

$$M_p = \sum_{i=1}^3 \left[\int_0^D L \cdot P_i \cdot (w + r + t_b) dw \right] \quad (20)$$

in which P_i represents the pressure in each set of chamber and w is the distance between G and the bottom of a sub-chamber (shown in Fig. 4(c)).

The third step is to establish the equilibrium with the moments caused by material resistance (M_s) and input air pressure (M_p). If the roll-down deformation is considered as pure bending of a cube, comparably, the external torque required to sustain such bending deformation without loading air pressure to chambers should be expressed as [38]

$$M_0 = \frac{1}{2}(r_1^2 - r_0^2)W(r_0) - \int_{r_0}^{r_1} RW(R)dR \quad (21)$$

in which $r_0 = r$, $r_1 = r + h$, R stands for the distance between the centre of pure bending O and point E within the robotic tongue body (shown as OE in Fig. 4(d)). The strain-energy function W is presented as

$$W(R) = C_1(I_1 - 3) + C_2(I_2 - 3) \quad (22)$$

in which

$$\begin{aligned} I_1 &= \left(\frac{r_0 r_1}{R}\right)^2 B^2 + (RB)^2 + C^2, \\ I_2 &= \left(\frac{R}{r_0 r_1 B}\right)^2 + \left(\frac{1}{RB}\right)^2 + \left(\frac{1}{C}\right)^2, \\ A &= \frac{r_1^2 - r_0^2}{2h}, B = \frac{A}{r_0 r_1}, C = \frac{1}{AB}. \end{aligned} \quad (23)$$

From Eqs. 19, Eq. 20, Eq. 21, Eq. 22 and Eqs. 23, it is found that M_p is the function of input air pressure P and deformation radius r while M_0 and M_s are only related to r . According to equivalence principle, the equilibrium is expressed as

$$M_0(r) = M_p(P, r) - M_s(r). \quad (24)$$

In bending deformation, the upper surface of the robotic tongue elongates, while the lower surface shortens. Approximately, the initial total length l (regarded as the average arc length) is used to calculate the bending angle θ in Eq. 25. Through simultaneous equations (Eq. 24 and Eq. 25), the relationship between input air pressure P and output bending angle θ is finally acquired.

$$\theta = \frac{l}{r} \quad (25)$$

C. DYNAMIC MODEL

Based on the proposed theoretical model for elongation and roll deformation above, dynamic model for these two simple deformation types can be acquired accordingly.

From previous modelling, the relationship between the output deformation and input air pressure is obtained, which can be expressed as

$$\lambda = \lambda(P); \theta = \theta(P). \quad (26)$$

Then by taking the derivative of Eqs. 26 with respect to time T , the equations can be changed to

$$\frac{d\lambda}{dT} = \frac{d[\lambda(P)]}{dP} \cdot \frac{dP}{dT}; \frac{d\theta}{dT} = \frac{d[\theta(P)]}{dP} \cdot \frac{dP}{dT}. \quad (27)$$

If the input air pressure P is a function of time T and continuous,

$$P = P(T) \quad (28)$$

Eqs. 27 can be further expressed as

$$\begin{aligned} \frac{d\lambda}{dT} &= \frac{d[\lambda(P)]}{dT} = \frac{d[\lambda(P)]}{dP} \cdot \frac{dP(T)}{dT}, \\ \frac{d\theta}{dT} &= \frac{d[\theta(P)]}{dT} = \frac{d[\theta(P)]}{dP} \cdot \frac{dP(T)}{dT}. \end{aligned} \quad (29)$$

In Eqs. 27, the left side of the equations can be regarded as the deformation velocity. Thus, as long as the input air pressure is given, both of the output deformation amount and deformation velocity can be calculated.

D. CONTROL ALGORITHM

The purpose of modelling the robotic tongue is to better understand the working performance and then try to control the movements of the robotic tongue. Four types of tongue movements can be divided into two categories. One is simple movement corresponding to roll-up, roll-down and elongation. The relationship between the input air pressure and output deformation can be simply described through the proposed theoretical model. The other is complicated movement corresponding to groove. The mechanical model of groove movement is difficult to set up due to its complicated shape

under deformation. The proposed mechanical model is not suitable for this type of movement.

For simple movement, the input air pressure can be acquired through the mechanical model based on the required tongue shape. The output deformation can be simply described as bending angle or elongation ratio. For complicated movement (groove), two key problems need to be solved. The first problem is how to describe the groove shape quantitatively. In previous work [28], the method of surface reconstruction was proposed to describe the robotic tongue surface quantitatively under any type of deformation using nine control points distributed evenly on the surface of the robotic tongue. Thus the quantitative description of groove shape can be realized through surface reconstruction. The second problem is how to find the relationship between the input air pressure and output groove deformation. Data-based model (e.g., Artificial Neural Network, ANN) can be used to build the bridge between the input air pressure and output complicated shape. The ANN can be trained using the experimental data obtained in Section IV. Based on the proposed mechanical model and data-based model (ANN), a closed-loop control algorithm of four types of tongue movements in speech is preliminarily designed as follows (Fig. 5).

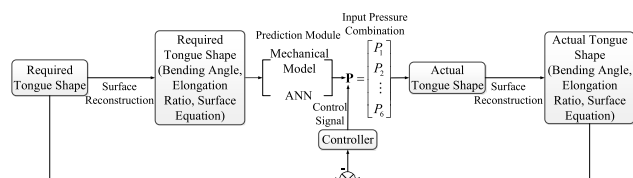


FIGURE 5. Control algorithm of the robotic tongue.

First of all, the required shape of the robotic tongue is converted to surface equation through surface reconstruction method. Meanwhile, deformation parameters such as bending angle and elongation ratio can also be acquired through the control points used in surface reconstruction. Then the required pressure combination in six sets of chambers can be obtained through mechanical model or trained ANN. By exerting the required pressure to chambers, the actual shape of the robotic tongue forms. Repeating the first step, surface equation, bending angle and elongation ratio of actual tongue shape can be obtained in line with different deformation types. Next, control signal is generated by controller according to the comparison between the actual shape and required shape of the robotic tongue after quantification. At last, control signal is used to regulate the input air pressure for the purpose of obtaining more accurate tongue shape. At this stage, research on the control algorithm especially the controller is still in progress, and more details may be published later.

IV. EXPERIMENTAL VERIFICATION

In order to verify the theoretical model, test the deformation repeatability in a relative long period of time, ANN based

control model and robotic tongue movements in speech, input air pressure and output deformation of the robotic tongue are recorded simultaneously in the experiment.

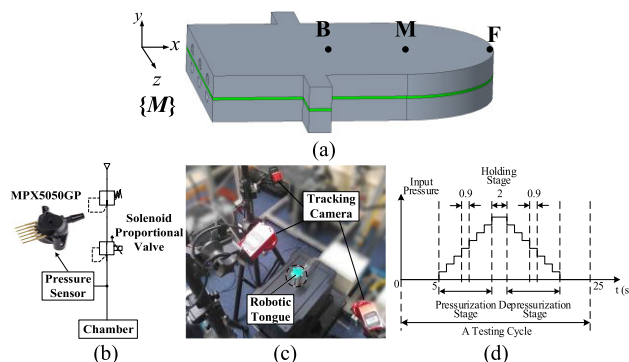


FIGURE 6. (a) The location of three markers and axes direction of measurement frame {M}; (b) The location of pressure sensor; (c) The motion tracking system (OptiTrack); (d) Testing cycle of the experiment.

A. EXPERIMENTAL SETUP

In order to obtain the parameters of six sets of chambers during experiments, three markers (F, M and B, shown in Fig. 6(a)) which are placed on the surface of the robotic tongue corresponding to the location of three key points in TABLE 1 and 6 pressure sensors (MPX5050GP) which locate between the solenoid proportional valve and chamber in pneumatic circuit (shown in Fig. 6(b), only one of six airways is presented) are added to the experimental setup based on the actuation and control system shown in Fig. 2. Motion tracking system (OptiTrack) is used to capture the motion of three markers (shown in Fig. 6(c)). A measurement frame {M} is defined during the calibration of OptiTrack system (shown in Fig. 6(a)). The x axis of {M} is along the elongation direction while the y axis is along the thickness direction of the robotic tongue. The displacement of three markers in {M} is recorded and sent to PC for further analyses. At the same time, input air pressure in chambers is measured by pressure sensors and recorded by PC through PCIe6321. By adding pressure sensors to the original actuation and control system (shown in Fig. 2), the experimental setup is able to acquire real-time pressure data in chambers. PC guarantees the synchronicity of the displacement signal and pressure signal.

The sampling frequency of both OptiTrack system and pressure sensor is 100 Hz. A testing cycle is set to 25 s containing three stages from the initial state to the largest deformation state and then back to the initial state (shown in Fig. 6(d)). When a testing cycle starts, OptiTrack system begins to record the coordinates of markers in {M}, triggering the acquisition of pressure signal through PC. The OptiTrack system and pressure sensors finish signal collection when testing time reaches 25 s. Thus a testing cycle ends.

The whole experimental process contains four parts including the verification of theoretical model, the test of

deformation repeatability, test of ANN based control model, and the test of robotic tongue movements in speech.

B. VERIFICATION OF THEORETICAL MODEL

In the experiment, OptiTrack system records the real-time coordinates of marker F in $\{M\}$ which are further converted to real-time bending angle θ and axial elongation λ . At the initial state, the coordinate of marker F in $\{M\}$ is defined as $F_0(x_0, y_0, z_0)$ which is acquired directly from OptiTrack system. At moment T , the coordinate of marker F in $\{M\}$ is $F_T(x_T, y_T, z_T)$. Then the variation of coordinate during the deformation process is expressed by Eqs. 30.

$$\Delta x = x_T - x_0, \Delta y = y_T - y_0, \Delta z = z_T - z_0. \quad (30)$$

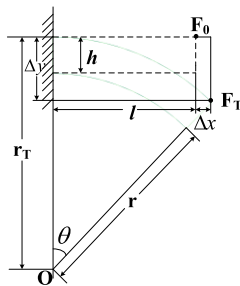


FIGURE 7. Geometrical relationship in roll-down deformation.

Due to the geometrical similarity of roll-up and roll-down deformation, roll-down is taken for instance. The geometrical relationship between the initial tongue and deformed tongue is shown in Fig. 7. It is assumed that the contour of the deformed robotic tongue is a portion of a circle with centre O and outer radius $OF_T = r_T$. Compared with the deformation range, the size of marker F is ignored. According to the geometrical relationship in Fig. 7, Eq. 31 is obtained.

$$(r_T - \Delta y)^2 + (l + \Delta x)^2 = r_T^2 \quad (31)$$

In Eq. 31, $l = 34.95$ mm represents the initial length of the robotic tongue without root part. The outer radius r_T is calculated as

$$r_T = \frac{\Delta y^2 + (l + \Delta x)^2}{2\Delta y}. \quad (32)$$

As mentioned above, the upper surface of the robotic tongue elongates, while the lower surface shortens in bending deformation. The initial total length l can be used to calculate the bending angle θ approximately. Also, during roll-down deformation process, the variation of tongue thickness is negligible. As a result, the bending angle θ at random moment T can be calculated using the initial total length l and inner radius r ($r = r_T - h$) based on Eq. 25.

$$\theta = \frac{l}{r} = \frac{l}{r_T - h}. \quad (33)$$

As to elongating, the direction of elongation is the same as x axis of $\{M\}$. Thus the elongation λ at random moment T is

directly acquired through the ratio of coordinate variation along x axis Δx and initial length l , that is

$$\lambda = \frac{\Delta x}{l}. \quad (34)$$

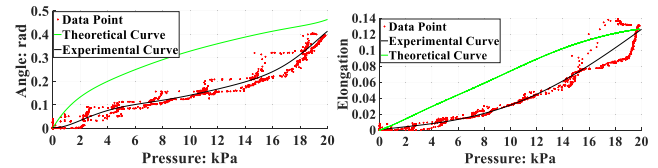


FIGURE 8. Comparison between theoretical and experimental data.

Aiming to present the relationship between the actual pressure in each pressurized chamber set and bending angle as well as elongation, theoretical and experimental curves are plotted respectively in Fig. 8. According to Eq. 33 and Eq. 34, experimental curves ($P-\theta$ and $P-\lambda$) are plotted by utilizing the coordinate data of marker F and pressure data in chambers obtained from pressure sensors. For the proposed theoretical model, corresponding $P-\theta$ and $P-\lambda$ curves are acquired through numerical method based on Eq. 24 and Eq. 13. Although the chambers are pressurized with same pressure, there exist unobvious differences among the actual pressures in different chamber sets due to the characteristic of silicone rubber material and fabrication error. The mean CV (Coefficient of Variation) of the pressures during the whole testing cycle is 9.68% which is acceptable. For convenience, the average of actual pressures is used to plot the experimental curves, and the exerted pressures in different chambers are set to be equal when plotting the theoretical curves.

In Fig. 8, green curves represent the theoretical curves ($P-\theta$ and $P-\lambda$) based on Mooney-Rivlin strain-energy function model; red dots represent the actual data points in experiment; black curves represent the polynomial fitted curves based on actual data points.

By comparing and analysing the relevance and difference between the theoretical curves and experimental curves, it is concluded as follows.

(1) Both the theoretical and experimental curves show that the bending angle θ and elongation λ increase monotonically with increasing pressure. However, significant difference between the theoretical and experimental curves does exist especially during the pressurization and depressurization stage.

(2) Under the same pressure, the deformation of theoretical model is larger than that in experiment. There are two main reasons resulting in such phenomenon: one is the deformation delay caused by the characteristic of silicone rubber material; the other is the model simplification. Specifically, friction and PDMS layer can both reduce the deformation amount. The negligence of these two factors in modelling causes the gap enlargement between the theoretical curve and experimental curve.

(3) With the increase of pressure, the difference between theoretical curve and experimental curve increases first and

then decreases mainly due to the deformation delay compared with pressure signal. During pressurization and depressurization stage, the time when pressure remains constant is too short for the deformation to reach stable state. However, during holding stage, pressure holding time is longer so that there is enough time for the deformation to approach or reach stable state. As a result, the experimental data is much closer to the corresponding theoretical data when the pressure approaches the maximum value.

(4) Hysteresis exists during pressurization and depressurization process.

During pressurization and depressurization stage, the error of theoretical data relative to experimental data is close to 100%. Nevertheless, the relative error is much smaller during holding stage. The minimum error is only 9.5% for bending and 1.6% for elongation. This is a common phenomenon which can be found in most soft actuators mainly due to the elastic material characteristic and compliant actuation pattern (e.g. pneumatic). According to the experimental results, it can be concluded that this mechanical model generally conforms to the actual relationship between the input air pressure and output deformation. Particularly, this model is able to describe the pressure-deformation relationship precisely in static state. However, the ability of dynamic prediction is not as satisfying as that of static prediction. From the analyses above, it can be inferred that the difference between theoretical data and experimental data will further decrease when pressure holding time is long enough. When controlling tongue shape in circumstances like pronunciation teaching device, we pay more attention to deformation results rather than deformation process. As a result, the proposed theoretical model is qualified in controlling tongue shape in static circumstances.

C. TEST OF DEFORMATION REPEATABILITY

Deformation fluctuation refers to the displacement variation of key points on tongue surface (e.g. marker F) under the same pressure during a relative long period of time, which is crucial to working stability and controllability. In order to test the deformation repeatability of the robotic tongue, deformation fluctuation is measured based on OptiTrack system.

Roll-down deformation is taken for instance to test the repeatability. The location of marker F is the same as that in Fig. 6(a). The whole experimental process lasts for 60 days. The coordinate data of marker F and the pressure data obtained from pressure sensors are recorded every 15 days (five times in total). Each time the 25 s testing cycle mentioned above is repeated for 15 times and the average is applied in data analysing and curve plotting later. For the purpose of further increasing the reliability and accuracy of recorded data, the testing system and environment including all hardwares, surrounding temperature and humidity remain the same during the whole experimental process.

The real-time displacement s of marker F along y axis is acquired through the recorded location of F in $\{M\}$. By utilizing polynomial fitting, the relationship between air

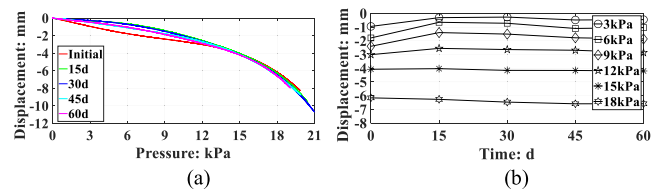


FIGURE 9. Experimental curves in long-term tracking: (a) $p-s$ curves; (b) $t-s$ curves.

pressure p in chambers and displacement s is further plotted as pressure-displacement curve ($p-s$ curve for short). Three chamber sets are involved in roll-down deformation and the average of pressures in three chamber sets is used to plot the $p-s$ curve. During the 60-day experiment, five $p-s$ curves are plotted in Fig. 9(a) corresponding to five-time recording process. From the consistency of the curves in Fig. 9(a), it is preliminarily concluded that the deformation repeatability of the robotic tongue during 60-day test is excellent, especially under higher pressures.

In order to further investigate the relationship between the deformation repeatability and recording time, $t-s$ curves (t represents the recording time during the whole experimental process, s represents the displacement of marker F along y axis in $\{M\}$) are plotted in Fig. 9(b). Based on the curves in Fig. 9(a), five data points are obtained from five curves under the pressure of 3 kPa, 6 kPa, 9 kPa, 12 kPa, 15 kPa and 18 kPa respectively. Utilizing these data points, six $t-s$ curves under six different pressures are acquired (shown in Fig. 9(b)).

TABLE 2. The SD of the displacements under different pressures.

Pressure (kPa)	3	6	9	12	15	18
SD of displacement (mm)	0.27	0.45	0.39	0.18	0.07	0.19

From Fig. 9(b), it is concluded as follows. At the beginning (before 30 days), the deformation fluctuation is relatively large compared with that in later period (after 30 days), especially under low pressures. Furthermore, the deformation fluctuation is quantitatively described using the standard deviation (SD) of the displacements based on the curves in Fig. 9(b). The SD of the displacements under different pressures is illustrated in TABLE 2. The maximum SD of the displacement is 0.45 mm when the pressure is 6 kPa, while the minimum is only 0.07 mm when pressurized with 15 kPa. In comparison with the displacement of marker F along y axis, the deformation fluctuation is negligible, which proves that the robotic tongue can still remain high deformation repeatability and controllability in long-term use.

D. TEST OF ANN BASED CONTROL MODEL

In order to acquire more precise data of all deformation types to train the ANN, further experiments are carried out. Based on the experimental setup above, more markers (nine in total)



FIGURE 10. The nine markers on the robotic tongue surface.

corresponding to the nine control points [28] are placed evenly on the surface of the robotic tongue and more testing cycles are repeated (shown in Fig. 10). The motion tracking and data recording process remains the same as mentioned in Section IV-A. Utilizing the deformation data of markers and pressure data in chambers, a double-layer feedforward ANN is trained. During deformation control, target deformation data is input to ANN through which required pressure data is obtained.

Motion tracking results of four deformation types including three simple types (roll-up, roll-down and elongation) and one complex type (groove) are obtained to train the ANN. Roll-up deformation is taken for instance. When training the ANN, the input object is the coordinate data of nine markers in $\{M\}$, while the output object is the pressure data of three pressurized chamber sets. Considering that a testing cycle is 25 s and the sampling frequency is 100Hz, the input object (3D coordinates of nine markers) is written as a 2501×27 matrix \mathbf{X}_1 , and the output object is written as a 2501×3 matrix \mathbf{X}_2 . For the purpose of accelerating convergence speed of the network and avoiding numerical problems, the input matrix \mathbf{X}_1 and the output matrix \mathbf{X}_2 is normalized before training the ANN. The normalized matrixes are defined as \mathbf{Y}_1 and \mathbf{Y}_2 corresponding to \mathbf{X}_1 and \mathbf{X}_2 respectively. The normalization process is expressed by

$$y = \frac{(y_{\max} - y_{\min})(x - x_{\min})}{x_{\max} - x_{\min}} + y_{\min} \quad (35)$$

in which x represents the element in \mathbf{X}_1 and \mathbf{X}_2 , y represents the element in \mathbf{Y}_1 and \mathbf{Y}_2 , x_{\min} , x_{\max} , y_{\min} and y_{\max} stand for the minimum and maximum elements of the corresponding matrix, $y_{\max} = 1$ and $y_{\min} = B-1$.

The feedforward ANN has two layers including hidden layer with sigmoid neurons structure and output layer with linear neurons structure. After balancing training time and accuracy, the number of hidden neurons is set to be 100. Although the structure is simple, the trained ANN is able to solve complicated problems such as multidimensional mapping and nonlinear processing.

After ANN training, the next step is accuracy verification of the trained ANN. During former training process, the data of only one testing cycle (defined as Cycle I) is used. Thus, another set of data of a second testing cycle (defined as Cycle II) is chosen to verify the trained ANN. The coordinate data from Cycle II is input to the trained ANN and the output predicted pressure data is compared with the actual pressure data from Cycle II (shown in Fig. 11(a)).

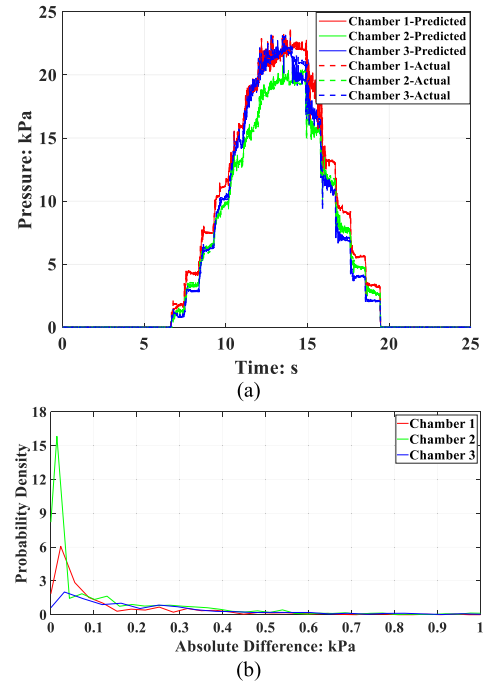


FIGURE 11. (a) Comparison between ANN predicted pressure and actual pressure; (b) The probability density distribution of difference e .

In Fig. 11(a), the curves of three different colours represent the relationship between the pressures in three chamber sets and testing time in Cycle II. The predicted data based on ANN and actual experimental data of the same chamber set are plotted in the same colour with different line patterns. From Fig. 11(a), it is found that high coincidence exists between the ANN predicted curves and experimental curves. In order to further describe the difference between the predicted data and actual data, probability density function is used. At each sampling point, the absolute difference e between the predicted pressure and actual pressure is calculated. The probability density distribution of difference e in a whole testing cycle is presented in Fig. 11(b).

In Fig. 11(b), the curves of three different colours stand for the probability density distribution of difference e in three pressurized chamber sets corresponding to the curves in Fig. 11(a). From the peaks of three curves in Fig. 11(b), it is found that the majority of the difference between the predicted and actual data is less than 0.1kPa in a whole testing cycle, which proves that the trained ANN is able to predict required pressure data based on control target precisely. Through the same training and verifying process, the ANN training results of other three deformation types also show high precision in data prediction. It has been proved in Section IV-C that the deformation repeatability of the robotic tongue is high. As a result, if the predicted pressures are exerted to chambers, the corresponding deformation should be close to target deformation. Coordinating with data feedback, the ANN based model is qualified in precise control of all deformation types. Particularly, this model can overcome the shortage of the delay in deformation control based

on mechanical model and be used in circumstances where dynamic control is required (e.g. humanoid robot).

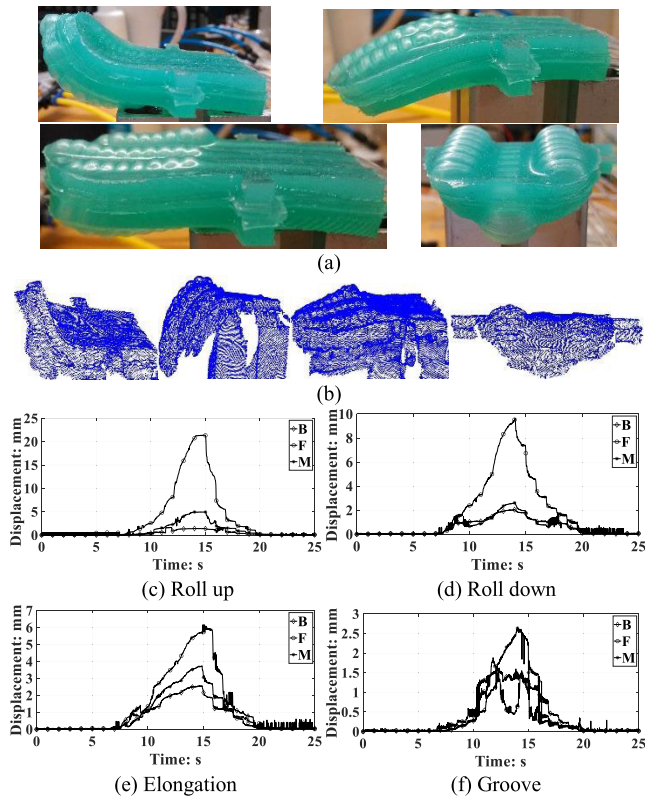


FIGURE 12. (a) Photos of deformed tongue; (b) The outline of deformed tongue through laser scan; (c), (d), (e) & (f) Motion tracking results of robotic tongue movement.

E. TEST OF ROBOTIC TONGUE MOVEMENTS IN SPEECH

Four simple types of movements including roll-up, roll-down, elongation and groove are achieved through the pressurization of different chamber set combinations (shown in Fig. 12(a)). In order to acquire real tongue shape under pressurization, the outline of deformed robotic tongue is obtained through static laser scan (shown in Fig. 12(b)). The laser scanner is selected as Konica Minolta VIVID 910 which is a 3D laser scanning system best at capturing high detail areas of non-moving objects and transferring the scanned object into more than 300000 points within 2.5 s with the highest accuracy of ± 0.008 mm. Although laser scanning is able to provide the outline of the robotic tongue precisely, it is not qualified in recording the whole deformation process due to its static property. Besides, it is difficult to relocate the exact key points (B, M and F) among the massive transferred points on the tongue surface after deformation.

Then, 3D motion tracking system OptiTrack is used to track and record the real-time coordinate of three key points during the whole phase of each movement. For four types of movements, the displacements of the markers (B, M and F) corresponding to time are shown in Fig. 12(c), (d), (e) and (f).

From Fig. 12(c), (d) and (e), it can be observed that the deformation of the robotic tongue generally accords with the regulation that the range decreases from the tongue tip to the root. Especially, the deformation of the tongue tip is much larger than that of the middle and root part. For roll-up, the maximum displacement of the tip (F) reaches 21.9 mm which is larger than the technical demand (20 mm). For roll-down and elongation, the maximum displacements are 10 mm and 6 mm respectively which are a little smaller than the requirement due to the deformation hysteresis and insufficient pressurization time. Similar to the experimental results of mechanical model verification above, the pressure in chambers starts to drop before the robotic tongue finishes deforming. Likewise, if enough pressurization time is provided, it can be inferred that the maximum displacement of roll-down and elongation will be close to or even reach the technical demand.

Compared with roll-up, roll-down and elongation, the deformation of groove is more complicated. During the groove deformation, the maximum displacement is about 3 mm at the middle part of the tongue (M), while the maximum displacements of the root part (B) and the tip (F) are almost the same (about 2 mm). For the reason that the tongue tip moves downwards (along $-y$ direction) first and then upwards (along $+y$ direction) during the deformation process, the resultant displacement accordingly increases first, and then decreases, finally increases again. There also exists difference between the experimental result and technical demand in groove deformation. However, the problem of insufficient pressurization time exists in groove deformation as well. Thus if the pressurization time and pressure in chambers increase during deformation process, the displacement of different part of the robotic tongue may increase accordingly and be closer to the technical demand. In addition, it can be seen from the deformed tongue photo and laser scan result in Fig. 12(a) & (b) that the general outline of the robotic tongue under groove deformation is consistent with the biological tongue shape in speech, which generally meets the demand in demonstrating the tongue shape when speaking.

V. CONCLUSION & DISCUSSION

A soft robotic tongue is proposed for the purpose of presenting typical tongue movements in speaking. During pronunciation training, the robotic tongue can provide more vivid tongue shapes for the hearing impaired. When the robotic tongue is mounted into the mouth of a humanoid robot and moves along with the mouth, such humanoid robot will acquire more verisimilitude. The robotic tongue is simplified from a biological tongue with three-layer structure and embedded chambers. It is driven by a pneumatic system which mainly contains air source, solenoid proportional valves, motion tracking system (OptiTrack), DAQ card (PCIe6321) and PC.

In order to further investigate the deformation characteristics of the robotic tongue, a theoretical model based on continuum mechanics is established. Two types of model

are included respectively for two typical deformation types which are elongation and roll. For elongation, this model is able to build the relationship between input air pressure and output elongation ratio; while for roll deformation, the relationship between actuation pressure and bending angle is described through this model. Furthermore, dynamic model is derived from the proposed model explaining the relationship between the deformation velocity and input air pressure. An integrated control algorithm is preliminarily proposed for different purpose of use based on the proposed theoretical model and ANN.

Based on the pneumatic actuation system, pressure sensor (MPX5050GP) is added to form the experimental setup. The experiments are divided into four parts: verification of theoretical model, test of deformation repeatability, test of ANN based control model and test of robotic tongue movements in speech. The experimental results of theoretical model verification show that the minimum error of theoretical data relative to experimental data is only 9.5% for bending and 1.6% for elongation indicating that the proposed theoretical model is qualified in controlling tongue shape statically. The controllability of the robotic tongue in a relative long period of time is tested through experiments on 60-day repeatability of deformation. It is found that the deformation repeatability of the robotic tongue during 60-day testing cycle is excellent, especially under higher pressures. The minimum deformation fluctuation is 0.07 mm. ANN based control model is trained and further verified through experimental data. The results show that this model is adequate to precise motion control of all deformation types. Particularly, ANN based control model is able to overcome the shortage of the delay in deformation control based on mechanical model, which is more suitable for dynamic motion control. By comparing the displacements of three key points (F, M and B) with medical measurements in references, it is found that the movements of robotic tongue generally meet the demand in demonstrating the tongue shape when speaking.

When using mechanical model based control method, the required input air pressure can be obtained directly through the deformation-pressure relationship. There is no need to carry out any pre-experiments. The only probable work before control is to adjust the geometrical parameters according to a different actuator. However, the common characteristic of most soft actuators that deformation delay exists compared with input air pressure is the main defect restricting the precision and application of this control model. In short, it is better at static control. For example, when presenting tongue shape in pronunciation training for the hearing impaired, both trainers and trainees are more curious about the static tongue shapes corresponding to different pronunciations. ANN based model can cover the shortage of deformation delay and provide dynamic and precise control for more deformation types. Nevertheless, a series of experimental data is required to train the ANN each time before starting to control a new actuator. This model is more suitable for controlling complicated tongue movements dynamically

along with the mouth of humanoid robot. The deformation process is the main focus in such circumstances.

In the future, the robotic tongue will be mounted into the mouth of humanoid robot or pronouncing demonstration device coordinating with other oral organs including teeth, palate and lip. It is challenging to set up the theoretical model of complicated deformation types (e.g. groove). Also, the defect of deformation delay does exist. Thus the proposed theoretical model along with other data-based methods (e.g. ANN) will be considered when designing full control scheme for wider application field. In addition, structural improvement of the robotic tongue will be carried on for the purpose of obtaining more deformation types and better deformation performance. Also embedding sensing system into the robotic tongue body using stretchable sensors and circuit will be taken into account.

REFERENCES

- [1] R. Becker and C. Artelt, "Evaluation of a training program using visible speech in German schools for the deaf," *J. Deaf Stud. Deaf Educ.*, vol. 3, no. 2, pp. 157–172, Apr. 1998.
- [2] T. Kawamura, T. Tandai, and H. Takanobu, "Mechanism and control of tongue robot," in *Proc. IEEE/RSJ Int. Conf. Intell. Robots Syst.*, Aug. 2005, pp. 1041–1046.
- [3] K. Nishikawa, H. Takanobu, T. Mochida, M. Honda, and A. Takanishi, "Modeling and analysis of elastic tongue mechanism of talking robot for acoustic simulation," in *Proc. IEEE/RSJ Int. Conf. Intell. Robots Syst. (IROS)*, Las Vegas, NV, USA, Feb. 2003, pp. 2107–2114.
- [4] K. Fukui, Y. Ishikawa, K. Ohno, N. Sakakibara, M. Honda, and A. Takanishi, "Three dimensional tongue with liquid sealing mechanism for improving resonance on an anthropomorphic talking robot," in *Proc. IEEE/RSJ Int. Conf. Intell. Robots Syst.*, St. Louis, MO, USA, Oct. 2009, pp. 5456–5462.
- [5] H. Yang, M. Xu, W. Li, and S. Zhang, "Design and implementation of a soft robotic arm driven by SMA coils," *IEEE Trans. Ind. Electron.*, vol. 66, no. 8, pp. 6108–6116, Aug. 2019.
- [6] Z. Wang, D. Wang, Y. Zhang, J. Liu, L. Wen, W. Xu, and Y. Zhang, "A three-fingered force feedback glove using fiber-reinforced soft bending actuators," *IEEE Trans. Ind. Electron.*, vol. 67, no. 9, pp. 7681–7690, Sep. 2020.
- [7] J. Cao, W. Liang, Y. Wang, H. P. Lee, J. Zhu, and Q. Ren, "Control of a soft inchworm robot with environment adaptation," *IEEE Trans. Ind. Electron.*, vol. 67, no. 5, pp. 3809–3818, May 2020.
- [8] J. Shintake, V. Cacucciolo, H. Shea, and D. Floreano, "Soft biomimetic fish robot made of dielectric elastomer actuators," *Soft Robot.*, vol. 5, no. 4, pp. 466–474, Aug. 2018.
- [9] J. Lee, J. Kim, S. Park, D. Hwang, and S. Yang, "Soft robotic palm with tunable stiffness using dual-layered particle jamming mechanism," *IEEE/ASME Trans. Mechatronics*, vol. 26, no. 4, pp. 1820–1827, Aug. 2021.
- [10] N. W. Bartlett, M. T. Tolley, J. T. B. Overvelde, J. C. Weaver, B. Mosadegh, K. Bertoldi, G. M. Whitesides, and R. J. Wood, "A 3D-printed, functionally graded soft robot powered by combustion," *Science*, vol. 349, no. 6244, pp. 161–165, Jul. 2015.
- [11] S. Liu, F. Wang, Z. Liu, W. Zhang, Y. Tian, and D. Zhang, "A two-finger soft-robotic gripper with enveloping and pinching grasping modes," *IEEE/ASME Trans. Mechatronics*, vol. 26, no. 1, pp. 146–155, Feb. 2021.
- [12] R. Hashem, M. Stommel, L. K. Cheng, and W. Xu, "Design and characterization of a bellows-driven soft pneumatic actuator," *IEEE/ASME Trans. Mechatronics*, vol. 26, no. 5, pp. 2327–2338, Oct. 2021.
- [13] A. D. Marchese, C. D. Onal, and D. Rus, "Autonomous soft robotic fish capable of escape maneuvers using fluidic elastomer actuators," *Soft Robot.*, vol. 1, no. 1, pp. 75–87, Mar. 2014.
- [14] M. Cianchetti, M. Calisti, L. Margheri, M. Kuba, and C. Laschi, "Bioinspired locomotion and grasping in water: The soft eight-arm OCTOPUS robot," *Bioinspiration Biomimetics*, vol. 10, no. 3, May 2015, Art. no. 035003.

- [15] Y. Li, Y. Liu, K. Yamazaki, M. Bai, and Y. Chen, "Development of a soft robot based photodynamic therapy for pancreatic cancer," *IEEE/ASME Trans. Mechatronics*, vol. 26, no. 6, pp. 2977–2985, Dec. 2021.
- [16] M. T. Tolley, R. F. Shepherd, B. Mosadegh, K. C. Galloway, M. Wehner, M. Karpelson, R. J. Wood, and G. M. Whitesides, "A resilient, untethered soft robot," *Soft Robot*, vol. 1, no. 3, pp. 213–223, Sep. 2014.
- [17] R. F. Shepherd, F. Ilievski, W. Choi, S. A. Morin, A. A. Stokes, A. D. Mazzeo, X. Chen, M. Wang, and G. M. Whitesides, "Multigait soft robot," *Proc. Nat. Acad. Sci. USA*, vol. 108, no. 51, pp. 20400–20403, Dec. 2011.
- [18] S. A. Morin, R. F. Shepherd, S. W. Kwok, A. A. Stokes, A. Nemiroski, and G. M. Whitesides, "Camouflage and display for soft machines," *Science*, vol. 337, no. 6096, pp. 828–832, Aug. 2012.
- [19] R. V. Martinez, J. L. Branch, C. R. Fish, L. Jin, R. F. Shepherd, R. M. D. Nunes, Z. Suo, and G. M. Whitesides, "Robotic tentacles with three-dimensional mobility based on flexible elastomers," *Adv. Mater.*, vol. 25, no. 2, pp. 205–212, Jan. 2013.
- [20] F. Ilievski, A. D. Mazzeo, R. F. Shepherd, X. Chen, and G. M. Whitesides, "Soft robotics for chemists," *Angew. Chem.*, vol. 123, no. 8, pp. 1930–1935, Feb. 2011.
- [21] P. Polygerinos, Z. Wang, J. T. B. Overvelde, K. C. Galloway, R. J. Wood, K. Bertoldi, and C. J. Walsh, "Modeling of soft fiber-reinforced bending actuators," *IEEE Trans. Robot.*, vol. 31, no. 3, pp. 778–789, Jun. 2015.
- [22] Y. Fei and H. Xu, "Modeling and motion control of a soft robot," *IEEE Trans. Ind. Electron.*, vol. 64, no. 2, pp. 1737–1742, Feb. 2017.
- [23] E. H. Skorina, M. Luo, W. Tao, F. Chen, J. Fu, and C. D. Onal, "Adapting to flexibility: Model reference adaptive control of soft bending actuators," *IEEE Robot. Autom. Lett.*, vol. 2, no. 2, pp. 964–970, Apr. 2017.
- [24] A. D. Marchese, K. Komorowski, C. D. Onal, and D. Rus, "Design and control of a soft and continuously deformable 2D robotic manipulation system," in *Proc. IEEE Int. Conf. Robot. Autom. (ICRA)*, Hong Kong, May 2014, pp. 2189–2196.
- [25] X. Lu, W. Xu, and X. Li, "Concepts and simulations of a soft robot mimicking human tongue," in *Proc. 6th Int. Conf. Autom., Robot. Appl. (ICARA)*, Queenstown, New Zealand, Feb. 2015, pp. 332–336.
- [26] X. Lu, W. Xu, and X. Li, "PneuNet based control system for soft robotic tongue," in *Proc. IEEE 14th Int. Workshop Adv. Motion Control (AMC)*, Auckland, New Zealand, Apr. 2016, pp. 353–357.
- [27] X. Lu, W. Xu, and X. Li, "A soft biomimetic tongue-model reconstruction and motion tracking," *Proc. SPIE*, vol. 9797, Apr. 2016, Art. no. 97970Y.
- [28] X. Lu, W. Xu, and X. Li, "A soft robotic tongue—Mechatronic design and surface reconstruction," *IEEE/ASME Trans. Mechatronics*, vol. 22, no. 5, pp. 2102–2110, Oct. 2017.
- [29] S. Standing, *Gray's Anatomy*, London, U.K.: Churchill Livingstone, 2008.
- [30] M. Stone and A. Lundberg, "Three-dimensional tongue surface shapes of English consonants and vowels," *J. Acoust. Soc. Amer.*, vol. 99, no. 6, pp. 3728–3737, Jun. 1996.
- [31] C. Jiang, "Physiology based tongue modelling and speech synchronized animation synthesis," M.S. thesis, Dept. Automat., Univ. Sci. Technol. China, Hefei, China, 2015.
- [32] V. J. Napadow, R. D. Kamm, and R. J. Gilbert, "A biomechanical model of sagittal tongue bending," *J. Biomechanical Eng.*, vol. 124, no. 5, pp. 547–556, Oct. 2002.
- [33] H. Zheng, Y. Zhu, and L. Wang, "Chinese 3D articulatory movement synthesis and animation," *J. Integr. Technol.*, vol. 2, pp. 23–28, Jan. 2013.
- [34] S. Fujita, J. Dang, N. Suzuki, and K. Honda, "A computational tongue model and its clinical application," *Oral Sci. Int.*, vol. 4, no. 2, pp. 97–109, Nov. 2007.
- [35] K. M. Hiimae, J. B. Palmer, S. W. Medicis, J. Hegener, B. S. Jackson, and D. E. Lieberman, "Hyoid and tongue surface movements in speaking and eating," *Arch. Oral Biol.*, vol. 47, no. 1, pp. 11–27, Jan. 2002.
- [36] L. Ma, "Research of pronunciation motion observation system based on photoelectric sensor," M.S. thesis, College Intell. Comput., Tianjin Univ., Tianjin, China, 2014.
- [37] Y. Huang, Y. Wang, L. Xiao, H. Liu, W. Dong, and Z. Yin, "Microfluidic serpentine antennas with designed mechanical tunability," *Lab Chip*, vol. 14, no. 21, pp. 4205–4212, 2014.
- [38] Z. P. Huang, *Fundamentals of Continuum Mechanics*, 2nd ed. Beijing, China: Higher Education Press, 2012.



XUANMING LU received the B.E. degree in mechanical engineering and automation and the Ph.D. degree in mechanical engineering from the Nanjing University of Science and Technology, China, in 2010 and 2019, respectively. He is currently a Lecturer with the Industrial Technology Research Institute of Intelligent Equipment, Nanjing Institute of Technology. He was with the Faculty of Engineering, University of Auckland, New Zealand, on leave from the Nanjing University of Science and Technology, from 2013 to 2017, with a Doctoral Scholarship from the China Scholarship Council. His main research interests include soft robots, biomimetic robots, and pneumatic technology.



WEILIANG XU (Senior Member, IEEE) received the B.E. degree in manufacturing engineering and the M.E. degree in mechanical engineering from Southeast University, Nanjing, China, in 1982 and 1985, respectively, and the Ph.D. degree in mechatronics and robotics from the Beijing University of Aeronautics and Astronautics, Beijing, China, in 1988. He joined the University of Auckland, Auckland, New Zealand, in February 2011, as the Chair of mechatronics engineering. Before this appointment, he was a Professor of mechatronics (2007–2010), an Associate Professor (2005–2006), and a Senior Lecturer (1999–2004) with the School of Engineering and Advanced Technology, Massey University, New Zealand. Prior to coming to New Zealand, he was with the City University of Hong Kong, Hong Kong, from 1993 to 1998; the University of Stuttgart, Stuttgart, Germany, from 1990 to 1992; and Southeast University, China, from 1988 to 1989. His current research interests include advanced mechatronics/robotics, with applications in medicine and foods.

Dr. Xu is a fellow of the Institution of Professional Engineers of New Zealand. He has been serving as an Associate Editor for the IEEE TRANSACTIONS ON INDUSTRIAL ELECTRONICS, since 2003, and the *ASME Journal of Engineering and Science in Medical Diagnosis and Therapy*, since 2017. He was an Associate Editor of *IEEE Robotics and Automation Magazine*, from 2008 to 2009, and an Editor of the *International Journal of Intelligent Systems Technologies and Applications*, from 2005 to 2010.



XIAONING LI received the B.E., M.E., and Ph.D. degrees in fluid power transmission and control from the Harbin Institute of Technology, Harbin, China, in 1982, 1984, and 1989, respectively.

In 1989, he joined the Nanjing University of Science and Technology, Nanjing, China, where he is currently a Professor with the School of Mechanical Engineering. His current research interests include modeling, simulation, and control for advanced manufacturing systems and pneumatic control technology.

Dr. Li is the Vice Director of the Manufacturing Committee of the Chinese Automation Association. He is an Editor of the *Journal of Machine Tool and Hydraulics* and the *Journal of the Nanjing University of Science and Technology*.

...